Nanoscale

ROYAL SOCIETY OF CHEMISTRY

PAPER

View Article Online
View Journal | View Issue

Cite this: *Nanoscale*, 2021, **13**, 14713

Enhanced drug retention by anthracene crosslinked nanocomposites for bimodal imaging-guided phototherapy†

Xiaoshan Fan,‡[a] Lingjie Ke,‡[b] Hongwei Cheng, ‡[c] Hu Chen,[c] Zhiguo Li,[b] Enyi Ye, *[d] Xian-Jun Loh, [d] Yun-Long Wu, *[b] Gang Liu *[c] and Zibiao Li *[d,e]

Efficient drug delivery, multifunctional combined therapy and real-time diagnosis are the main hallmarks in the exploitation of precision nanomedicine. Herein, an anthracene-functionalized micelle containing a magnetic resonance imaging (MRI) contrast agent, upconversion nanoparticles (UCNPs) and the photosensitizer IR780 is designed to achieve sustained drug release and enhanced photothermal and photodynamic therapy. The polymer-coated hybrid micelle was achieved by crosslinking anthracene-dimer with UV light (λ > 300 nm), which is converted from near-infrared (NIR) irradiation upon UCNPs. Besides, the water-insoluble photosensitizer IR780 is introduced into the system to achieve efficient drug delivery and photothermal and photodynamic synergistic therapy. As a consequence of NIR-induced anthracene-dimer formation, the cross-linked nanocomposite shows sustained drug release, and the enhanced retention effect of IR780 could increase the photothermal conversion efficiency. Importantly, the incorporation of 2,2,6,6-tetramethyl-piperidineoxyl (TEMPO) as a nitroxide MRI contrast agent presents the potential for real-time diagnosis *via* nanotheranostics, and the fluorescence imaging of IR780 is applied to monitor drug distribution and metabolism. This strategy of sustained drug delivery by anthracene-dimer formation through the better penetration depth of NIR-II fluorescence provides an executable platform to achieve enhanced phototherapy in biomedical applications.

Received 28th June 2021,
Accepted 12th August 2021

DOI: 10.1039/d1nr04171a

rsc.li/nanoscale

Introduction

Phototherapeutics has been widely investigated in the diagnosis and treatment of diseases to improve the theranostic efficiency.[1,2] The diagnostic value of light-based materials is mainly achieved by disease-specific imaging, including fluorescence imaging (FLI) and photoacoustic imaging (PAI), with the characteristics of real-time, fast, high sensitivity and easy operation.[3,4] To achieve the improvement of cellular fluorescent probe uptake and prolong the drug retention time, many polymeric micelles and cell membrane vesicle materials are processed to optimize the drug delivery system (DDS).[5,6] For example, Evans blue and indocyanine green (ICG) are the common clinical drugs for nanomedicine manufacture. Evans blue, as a tracer with high affinity for plasma albumin, can be used to detect the integrity of the blood–brain barrier (BBB) of the nervous system.[7] ICG, as a diagnostic reagent, is applied for the detection of liver and blood vessel function by pathology-induced differential residence time.[8] Benefitting from the good biocompatibility, the imaging features of ICG have also been deeply investigated in the surgical navigation for tumor resection, and the on-demand resection is conducive to the prognosis of patients.[9,10] On the other hand, the efficacy of drug treatments, the photosensitizer-based innovative treatments, including photodynamic therapy (PDT) and photothermal therapy (PTT), is another important aspect which has great potential to improve the current treatment options, especially in cancer treatment.[11,12] With the assistance of photosensitizers and lasers, the photochemical reactions of PDT can generate reactive oxygen species (ROS) to achieve a minimally invasive

[a]*State Key Laboratory for Modification of Chemical Fibers and Polymer Materials, College of Materials Science and Engineering, Donghua University, Shanghai 201620, P. R. China*
[b]*Fujian Provincial Key Laboratory of Innovative Drug Target Research and State Key Laboratory of Cellular Stress Biology, School of Pharmaceutical Sciences, Xiamen University, Xiamen 361102, China. E-mail: wuyl@xmu.edu.cn*
[c]*State Key Laboratory of Molecular Vaccinology and Molecular Diagnostics & Center for Molecular Imaging and Translational Medicine, School of Public Health, Xiamen University, Xiamen 361102, China. E-mail: gangliu.cmitm@xmu.edu.cn*
[d]*Institute of Materials Research and Engineering, A*STAR (Agency for Science, Technology and Research), 2 Fusionopolis Way, Innovis, #08-03, Singapore 138634, Singapore. E-mail: yeey@imre.a-star.edu.sg, lizb@imre.a-star.edu.sg*
[e]*Department of Materials Science and Engineering, National University of Singapore, 9 Engineering Drive 1, 117576, Singapore*

†Electronic supplementary information (ESI) available. See DOI: 10.1039/d1nr04171a

‡These authors contributed equally to this work.

and toxic treatment.[13,14] As an extension of PDT, PTT can effectively convert photosensitizers from the ground state to an excited state, and thus release abundant heat; both these treatments exhibit excellent performance in tumor inhibition.[15,16]

Many defects restrict the clinical application of phototherapeutics, one among which is the poor delivery of photosensitizers. For example, ICG is a clinically-approved drug, and its rapid clearance and photoinstability limit its theranostic performance. An optimized near-infrared (NIR) fluorescent dye, IR780, shows better fluorescence capability with increased stability than ICG, which are potential advantages to overcome the current limitation of fluorescent dyes. Considering the insoluble property, some polymeric micelles were designed to load IR780 and deliver it to the tumor site by active targeting modification or nanocarrier-specific passive targeting. However, the dissociation behavior of polymeric micelles is still unclear, which might contribute to the unexpected therapeutic efficacy. Thus, *in vivo* behavior monitoring of micelles is a significant work to understand their therapeutic value. More importantly, the structures of micelles affect their drug delivery behavior. The micelles are generally in the shape of spheres, columns or sheets, and transformation from a monomer to a two-dimensional polymer is accompanied by a remarkable change in physical and chemical properties. For example, a cyclodextrin-based supramolecular hydrogel *via* UV-crosslinked anthracene dimerization controls the shear-thinning behavior.[17] Anthracene-functionalized polymer fibers exhibit robust mechanical strength, suggesting the potential biomedical value of the anthracene-functionalized polymer.[18]

To determine the pharmaceutical value of the anthracene-functionalized polymer in phototherapy, and achieve *in vivo* image monitoring, a light-responsive polymeric platform with magnetic resonance imaging (MRI) contrast capability is firstly reported. 2,2,6,6-Tetramethyl-piperidineoxyl (TEMPO) as an organic agent with the property of electron paramagnetic resonance (EPR) imaging is superior in theranostic evaluation. Furthermore, considering the limited penetration depth of UV, upconversion nanoparticles (UCNPs, NaYF4:Yb/Tm@NaYF4) composed of lanthanide elements are loaded along with IR780 into the integrated system, which can convert NIR-II excitation with good penetration depth[19,20] into UV emission, realizing NIR-controlled drug release and photosensitizer-induced PDT and PTT simultaneously (Scheme 1). In summary, a versatile strategy for an enhanced phototherapeutic outcome is developed to achieve a better tumor treatment effect with MRI/PA bimodal imaging guidance.

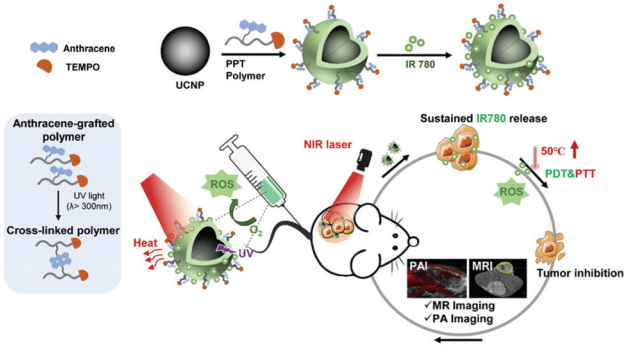

Scheme 1 The schematic diagram of anthracene crosslinked nanocomposites containing upconverting nanoparticles and IR780 for bimodal imaging-guided phototherapy.

Experimental

Materials and chemicals

Monohydroxyl poly(ethylene glycol) (mPEG-OH, M_n 5000) was purchased from Sigma Aldrich. Styrene (99%, Aladdin) was passed through a short column with neutral alumina oxide to remove the inhibitor just before use. Maleic anhydride (99%, Maklin), 9-anthracenecarboxylic acid (99%, Adamas), cystamine dihydrochloride (98%, Maklin), *N*-(3-dimethylaminopropyl)-*N*′-ethylcarbodiimide hydrochloride (EDC, 98.5%, Maklin), and 4-amino-2,2,6,6-tetramethyl-piperidinooxy (TEMPO-NH2, 98%, Aladdin) were used as received. The chain transfer agent (CTA) S-1-dodecyl-S′-(α,α′-dimethyl-α″-acetic acid)trithiocarbonate (DDAT) was synthesized according to a previous method. Tetrahydrofuran and chloroform were supplied by Sinopharm Chemical Reagent Co. Ltd. Tween 80 and Trypsin-EDTA were supplied by Solarbio Technology Co., Ltd. Phosphate buffered saline (PBS) was supplied by Beyotime Biotechnology Co., Ltd. Roswell Park Memorial Institute-1640 (RPMI-1640), Dulbecco's modified Eagle's medium (DMEM), penicillin–streptomycin and fetal bovine serum (FBS) were purchased from Thermo Fisher Scientific. DAPI-containing sealant, 3-(4,5-dimethyl-2-thiazolyl)-2,5-diphenyl-2-*H*-tetrazolium bromide (MTT), sucrose, hematoxylin & eosin (H&E) and terminal-deoxynucleotidyl Transferase Mediated Nick End Labeling (TUNEL) were obtained from Yeasen Biotechnology Co. Ltd. 2′,7′-Dichlorodihydrofluorescein diacetate (H2DCFDA) was supplied by MedChemExpress. Alkaline phosphatase (ALP), aspartate aminotransferase (AST), alanine aminotransferase (ALT), blood urea nitrogen (BUN) and albumin (Alb) detection kits were purchased from Nanjing Jiancheng Technology Co., Ltd.

Synthesis of mono Boc protected cystamine (Boc-SS-NH_2)

Boc-SS-NH_2 was synthesized according to the protocol reported in the literature. Briefly, cystamine dihydrochloride (5.98 g, 26.48 mmol) and triethylamine (13.6 mL, 85.36 mmol) were dissolved in methanol (50 mL). The solution was cooled to 0 °C in an ice-water bath, and then the methanol solution of Boc anhydride (5.98 g, 26.46 mmol) was added dropwise into the solution. The reaction mixture was allowed to stir at 0 °C for 30 min and another 4 h at room temperature. The solvent was removed under reduced pressure and the residue was washed with diethyl ether three times. The resultant solid was dissolved with 1 M NaOH aqueous solution, and then was extracted with ethyl acetate. A pale yellowish oil was obtained as the organic phase dried over magnesium sulfate was evaporated.

Synthesis of Boc-SS-An

Boc-SS-An was synthesized by the EDC/DMAP assisted esterification between Boc-SS-NH_2 and 9-anthracenecarboxylic acid. In a dried round bottom flask with a stir bar, Boc-SS-NH_2 (2.39 g, 6.78 mmol) and 9-anthracenecarboxylic acid (2.25 g, 10.17 mmol) were dissolved in 10 mL of anhydrous DMF. Under a nitrogen stream, EDC (1.95 g, 10.17 mmol) and DMAP (0.17 g, 1.35 mmol) were added into the flask. The reaction mixture was stirred overnight at room temperature. Next, the solution was diluted with DCM and washed with deionized water and saturated NaCl solution. The solvent was removed by evaporation under reduced pressure, and the resultant residue was purified by silica column chromatography with a mixture of hexane/ethyl acetate (1/1, v/v) as an eluent to obtain Boc-SS-An.

Synthesis of An-SS-NH_2

Deprotection of the Boc group on Boc-SS-An was performed in a solution of TFA/DCM. Briefly, Boc-SS-An (1.46 g) was dissolved in anhydrous DCM (5 mL) at 0 °C, and then TFA (1.0 mL) was added dropwise into the solution. After completion of the addition, the solution was allowed to stir for 3 h at room temperature. The solution was concentrated on a rotary evaporator, and then the residue was re-dissolved with DCM and washed with saturated aqueous $NaHCO_3$. The solvent was removed under reduced pressure affording the final product An-SS-NH_2, which was used for the next step without further purification.

Characterization of the copolymer by ^{1}H NMR, GPC and FTIR

mPEG-RAFT macro-CTA, mPEG-*b*-PSMAn and mPEG-*b*-P(SMA(-TEMPO)-SS-An were dissolved in $CDCl_3$, respectively, and ^{1}H NMR spectra of which were detected using a nuclear magnetic resonance system (JEOL JNM-ECA 500 MHz, JEOL, Japan) at room temperature. Fourier transform infrared spectra of mPEG-RAFT macro-CTA, mPEG-*b*-PSMAn and mPEG-*b*-P(SMA(-TEMPO)-SS-An were recorded using an FTIR system (Nicolet 380, Thermo Electron, USA). The physical properties of mPEG-RAFT and mPEG-*b*-PSMAn were measured using a Gel Permeation Chromatograph (GPC, Tosoh EcoSEC, Japan).

In vitro and *in vivo* optical characterization of the copolymer

The T1 magnetic resonance imaging of the PPT copolymer with different concentrations were detected by magnetic resonance imaging (MRI, Bruke 9.4T MicroMRI, Bruker, Germany). In order to verify the *in vivo* MRI effect, we monitored the imaging effect using MRI after the construction of the HepG2 solid tumor model by injecting the polymeric nanocomplex intravenously, and evaluated the T1 contrast capacity between the tumor and normal tissue. Due to the photoacoustic imaging ability of IR780, we also used an ultrasonic photoacoustic multimode imaging system (Vevo LAZR-X, FUJIFILM VisualSonics, Japan) to test the photoacoustic imaging capability of IR780 alone and PPTIU polymeric nanocomposites.

Synthesis of poly(ethylene glycol) macro-CTA (mPEG-CTA)

The macro-CTA was prepared *via* the esterification of monohydroxyl-terminated PEG with DDAT in the presence of EDC/DMAP catalysts. mPEG-OH (5.21 g, 1.04 mmol) was weighed into a previously dried 50 mL round-bottomed flask and dissolved in 40 mL of dried chloroform. DDAT (0.57 g, 1.56 mmol), EDC (0.30 g, 1.56 mmol) and DMAP (0.06 g, 0.51 mmol) were then added. The resulting solution was stirred at room temperature for 24 h. After being diluted with chloroform, the solution was washed successively with deionized water three times. The organic layer was dried over magnesium sulfate, concentrated on a rotary evaporator, and precipitated in cold diethyl ether two times. The macro-CTA as a light yellow powder was obtained after drying under vacuum.

Synthesis of poly(ethylene glycol)-*block*-poly(styrene-*alt*-maleic anhydride) (PEG-*b*-PSMAn) *via* RAFT polymerization

To a 25 mL Schlenk flask, mPEG-CAT (3.45 g, 0.65 mmol), St (2.35 g, 22.75 mmol), MAH (2.23 g, 22.75 mmol) and AIBN (0.02 g, 0.13 mmol; macro-CTA/initiator molar ratio = 5.0) were dissolved in 20 mL of 1,4-dioxane. The reaction solution was degassed by purging with nitrogen flow for 30 min at 0 °C. As being sealed with a rubber stopper, the flask was immersed into a preheated oil bath at 70 °C to start the polymerization. After 3 h, the polymerization was quenched by cooling the reaction mixture to ambient temperature. The solution was diluted with another 10 mL of 1,4-dioxane, and then precipitated into 5-fold excess of diethyl ether. The desired diblock copolymer PEG-*b*-PSMA was obtained after being dried *in vacuo* at 45 °C for 24 h.

Synthesis of PEG-*b*-P(SMA(-TEMPO)-SS-An)

PEG-*b*-P(SMA(-TEMPO)-SS-An) was obtained *via* the reaction of MAH units on the as-prepared PEG-*b*-PSMAn with 4-amino-2,2,6,6-tetramethyl-piperidinooxy (TEMPO-NH_2) and An-SS-NH_2. In brief, PEG-*b*-PSMAn (1.86 g, 0.18 mmol; 26 equiv. MAH), TEMPO-NH_2 (0.40 g, 2.36 mmol) and An-SS-NH_2 (0.83 g, 2.36 mmol) were dissolved in dry DMF (8 mL). The reaction lasted for 24 h at room temperature, and then for another 12 h at 110 °C. The solution was diluted with DCM and extracted with water three times. The concentration of the organic phase was obtained and the subsequent precipitation into diethyl ether two times was conducted to afford the product PEG-*b*-P(SMA(-TEMPO)-SS-An).

Preparation of IR780 loaded PPTI and PPTIU nanocomposites and IR780 encapsulation efficiency measurement

UCNPs (NaYF4:Yb/Tm@NaYF4) were provided by the School of Biomedical Engineering, Anhui Medical University. PPTIU nanocomposites were prepared by the solvent volatilization method. Firstly, UCNPs were centrifuged and precipitated using ethanol. The PPT polymer (10 mg) and UCNPs (10 mg) were separately dissolved in 100 μL of tetrahydrofuran and 100 μL of chloroform, and the mixtures were added dropwise into 2 mL of double distilled H_2O to form a PPTU emulsion.

Then organic reagent was removed by stirring vigorously at room temperature for 2 hours. After that, 1 mg of IR780 iodide was dissolved in 100 μL of methanol and the mixture was added dropwise into PPTU aqueous solution and stirred overnight in the dark. Then the obtained PPTIU nanocomposites were filtered through a dialysis bag (MWCO, 1000 Da) for 12 h to remove the unloaded free component and stored at 4 °C for further use. The PPTI was also prepared as a comparison in the same method except that UCNPs are not added. Also, HPLC (1290 Infinity II, Agilent, USA) was used to detect the concentration of free IR780 which was not loaded at the UV absorption wavelength of 790 nm, so as to obtain the IR780 encapsulation efficiency (EE (%), the weight of loaded IR780 in the obtained nanocomposites/weight of IR780 used × 100%).

Characterization of PPTIU nanocomposites

Time dependent UV absorbance spectra under UV irradiation (365 nm, 7 W cm^{-2}) of the PPT polymer were recorded using a multifunctional microplate reader (Multiskan FC, Thermo Fisher Scientific, USA). In order to verify that the temperature increase caused by the photothermal treatment of IR780 would not affect the cross-linking state of the PPT polymer, we also tested the UV absorption of the PPT polymer at 45 °C and 60 °C. The hydrate particle size and polymer dispersity index (PDI) were characterized using a dynamic light scattering zetasizer system (Nano S90, Malvern, UK). The nanomorphologies of UCNPs alone and UCNP and IR780 loaded PPTIU nanocomposites were obtained by transmission electron microscopy (TEM, G2 Spirit Biotwin, Thermo Fisher Scientific, USA). In order to evaluate the drug loading capacity of the PPT polymer, a series of micelle solutions containing different drug ratios (corresponding to PPT : UCNP : IR780) have been prepared to detect the fluorescence spectrum of IR780 (E_x = 700 nm) using a fluorescence spectrophotometer (Varian Eclipse, Varian, USA).

In vitro drug release ability

The concentration of IR780 was detected by HPLC at a UV absorption wavelength of 790 nm. The column used was C18 (4.6 × 250 mm, 3.5 μm), and the mobile phase consisted of 90% methanol and 10% water (containing 0.5% formic acid) with a flow rate of 0.9 mL min^{-1}. In order to detect the influence of the PPT polymer cross-linking state on drug release, we specifically set up two groups: the PPTU nanocomposite group under UV irradiation (365 nm, 7 W cm^{-2}) for 15 min and the no-UV irradiation PPTIU group. In detail, 1 mL of the nanocomposite solution was respectively placed in dialysis bags (MWCO, 3500 Da), and the release medium was PBS solution containing 1% Tween 80. The dialysis bag was placed in 19 mL of PBS dialysate and released in an environment of 37 °C and 100 rpm. 200 μL of samples were gathered at fixed time points, and 200 μL of fresh dialysis fluid was added to replace the samples, and the released IR780 concentration was detected by HPLC.

Cell culture

The HEK293T human embryonic kidney cell line and HepG2 human hepatocellular carcinoma cell line were cultured with RPMI-1640 medium, and LO2 human normal liver cell line was cultured with DMEM culture medium, both of which contained 10% of fetal bovine serum (FBS) and 1% of penicillin–streptomycin, and the culture conditions were 37 °C and 5% CO_2.

Cellular uptake of the PPTIU nanocomposites

The cellular uptake experiment was mainly aimed at exploring the intracellular IR780 uptake in HepG2 cells with the PPTIU complex, and IR780 with strong fluorescence was used as a fluorescent indicator. For one thing, the concentration of IR780 uptake by HepG2 cells was photographed using a confocal microscope (LSM5 EXCITER, Zeiss, Germany). IR780 and PPTIU (where IR780 has a concentration of 1 μg mL^{-1}) were cultured in 12-well plates containing 1×10^5 HepG2 cells for 0.5 h and 1 h. Then the supernatant of the 12-well plates was extracted before PBS washing 3 times and 4% paraformaldehyde fixing for 30 min. The tablet was sealed with a DAPI-containing sealant, and the DAPI-localized nuclei (E_x = 405 nm) and the fluorescence of IR780 (E_x = 633 nm) were imaged using a laser confocal microscope. The fluorescence intensity of IR780 was also detected by flow cytometry (Attune NxT flow cytometry, Thermo Fisher Scientific, USA). The culture method was the same as above, but the cell density was 2×10^5 HepG2 cells. Then the cells were digested with trypsin-EDTA, washed and suspended with PBS before measuring the fluorescence signal of IR780 upon 780 nm excitation by flow cytometry.

Evaluation of ROS production

To investigate the PPTIU nanocomposite-mediated reactive oxygen species (ROS) level, we use 2′,7′-dichlorodihydrofluorescein diacetate (H2DCFDA) as a fluorescent probe of ROS.[21] Firstly, HepG2 cells were cultured in a 24-well plate for 24 h to achieve a cell concentration of 1×10^5 cell per well, and then the medium was replaced with IR780 and PPTIU nanocomplex solution (IR780, 1 μg mL^{-1}) using cell culture medium as a solvent for another 1 h before adding an appropriate volume of H2DCFDA solution to make its final concentration reach 10 μM, and the cells were incubated for another 30 min. After that, the cells were irradiated with an 808 nm near-infrared laser for 5 min (1.5 W cm^{-2}), and the fluorescence signal of H2DCFDA was detected using a laser confocal microscope (E_x = 488 nm) and a fluorescence spectrophotometer (E_x = 405 nm).

Cell growth inhibition analysis

LO2 cells, HEK293T cells and HepG2 cells were cultured in a 96-well plate for 12 h to achieve a cell density of 5×10^3. UCNP, PPT, IR780, PPTI and PPTIU solutions with a concentration gradient were respectively used as solvents to add to the cells, and the incubation continued for 24 h. In addition, IR780 plus NIR, PPTI plus NIR, and PPTIU plus NIR groups were set up to explore the PDT effect of IR780 by near-infrared laser

irradiation at 808 nm. The old medium was replaced with MTT, and the UV absorption at 490 nm was measured using an absorbance microplate reader (CMAX PLUS, Molecular Devices, USA) to obtain the cell viability.

Construction of the tumor model

Male BALB/c nude mice were purchased from Shanghai Slake for the *in vivo* drug therapy effect evaluation experiment later. In order to construct a solid tumor model, we mainly injected a pre-cultured HepG2 cell PBS suspension (2×10^6 cells) subcutaneously. All animal procedures were performed in accordance with the Guidelines for Care and Use of Laboratory Animals of Xiamen University and experiments were approved by the Animal Ethics Committee of Xiamen University (XMULAC20190033).

Evaluation of *in vitro* and *in vivo* photothermal effects of PPTIU nanocomposites containing IR780

To evaluate the NIR photothermal response of IR780, we used an infrared thermal imager (Ax5, Beijing Junchuang Hongye Technology Co. Ltd, China) to monitor the temperature change of free PPTIU nanocomposites under NIR illumination (808 nm, 1 W cm^{-2}) in real time. In addition, when the tumor volume reached 150 mm^2, the PPTIU nanocomplex (IR780, 1 mg mL^{-1}) was injected into the tumor and the tumor site was irradiated with an NIR laser in the same step above to observe the temperature change trend of the subcutaneous tumor *in situ*.

Evaluation of the *in vivo* therapeutic efficacy of PPTIU nanocomposites

When the tumor volume reached about 100 mm^3, solid tumors were treated with 100 μL of normal saline, PPT, UCNP, IR780, PPTI and PPTIU nanocomposite groups containing PPT (10 mg kg^{-1}), UCNPs (10 mg kg^{-1}) and IR780 (1 mg kg^{-1}), respectively, by intra-tumoral injection. At the same time, IR780 plus NIR, PPTI plus NIR and PPTIU plus NIR groups were also set to evaluate the photothermal treatment effect, for which the tumor sites were irradiated with near-infrared light (808 nm, 1 W cm^{-2}) for 3 min after administration, and the irradiation was repeated the next day. During the period of treatment, the length and width of the tumor were measured with a Vernier caliper daily, and the weight of nude mice was also weighed using a scale. The tumor volume was calculated by the formula of (length × $width^2$)/2. After 11 days of treatment, the nude mice were sacrificed and the tumors, hearts, livers, spleens, lungs and kidneys were excised, and the tumor weight was weighed using a balance. The tissues were separated and placed in 10% formalin for fixation for 6 h, and then dehydrated with 15% sucrose for 24 h, and with 30% sucrose for 12 h. The tissue was frozen and sliced into tissue sections with a thickness of 6 mm using a freeze slicer (CM1900, Leica, Germany). The tissues were stained with hematoxylin and eosin for histological research. A positive fluorescence microscope (AXIO IMAGER AI, Zeiss, Germany) was used to observe H&E stained tissue sections.

Histopathological section and blood biochemical examination

To detect cell apoptosis, terminal-deoxynucleotidyl Transferase Mediated Nick End Labeling (TUNEL) was applied to label the nuclear DNA chain fracture, and then tissue sections were photographed using a laser confocal microscope. To evaluate the toxicity of PPTIU nanocomposites to the liver, kidneys and heart, the concentrations of alkaline phosphatase (ALP), aspartate aminotransferase (AST), alanine aminotransferase (ALT), blood urea nitrogen (BUN) and albumin (Alb) in the serum from the administration groups have been investigated to compare with healthy nude mice serum, and then to assess the presence of liver, kidney, and heart dysfunction and cellular damage.

Statistical analysis

All data are presented as mean ± standard deviation, and the difference between the two groups is obtained by Student's *t*-test. The *P*-value below 0.05 is considered as the significant difference.

Results and discussion

Synthesis and characterization of polymers

The functional copolymer PEG-*b*-P(SMA(-TEMPO)-SS-An) (the copolymer was named PPT) was successfully prepared according to the synthetic route shown in Fig. 1. The precursor PEG-*b*-PSMAn was first synthesized *via* RAFT polymerization using

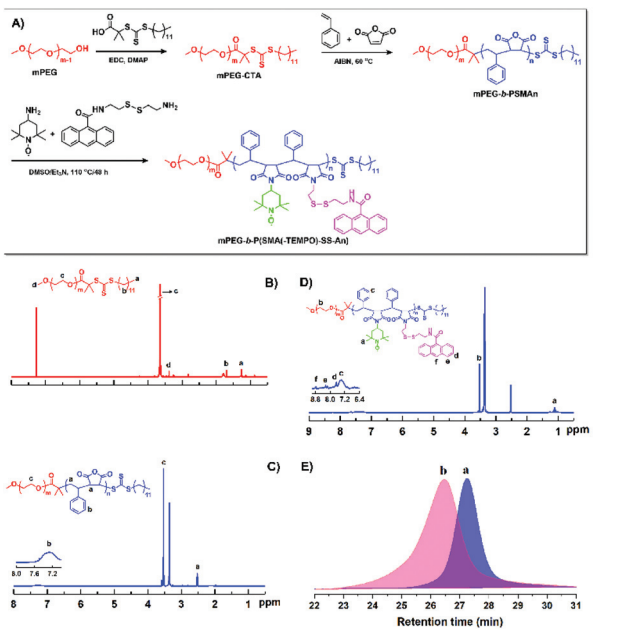

Fig. 1 Schematic illustration of the synthetic route (A) and characterization of mPEG-b-P(SMA(-TEMPO)-SS-An). ^{1}H NMR spectra of mPEG-RAFT macro-CTA in $CDCl_3$ (B), mPEG-*b*-PSMAn in DMSO-d_6 (C) and mPEG-*b*-P(SMA(-TEMPO)-SS-An in DMSO-d_6 (D), and (E) GPC traces of the polymers of mPEG-RAFT (a) and mPEG-*b*-PSMAn (b) with THF as an eluent.

mPEG-CTA as the macro-initiator. The aminolysis reaction between An-SS-NH2 and the anhydride group in the PSMAn block afforded the copolymer PEG-*b*-P(SMA-SS-An). The anhydride group in the PSMAn block reacted with An-SS-NH2 *via* the aminolysis reaction to obtain the copolymer PEG-*b*-P(SMA-SS-An), and the reactive carboxylic acid group was formed during the aminolysis reaction. The carboxylic acid group on the P(SMA-SS-An) block further reacted with TEMPO-OH *via* the EDC/DMAP assisted esterification to give the functional copolymer PEG-*b*-P(SMA(-TEMPO)-SS-An). The stable micelles self-assembled by PEG-*b*-P(SMA(-TEMPO)-SS-An) can be achieved as being crosslinked by UV illumination at 365 nm due to the [4 + 4] cycloaddition of the anthracene groups in the micellar core. Moreover, the stable radicals TEMPO and disulfide bonds in the core could endow the formed micelles with the properties of electron paramagnetic resonance (EPR) imaging and redox responsivity.

The obtained functional block copolymer PEG-*b*-P(SMA(-TEMPO)-SS-An) and the intermediates were well characterized by ^{1}H NMR, GPC and FT-IR techniques. Fig. 1C shows the ^{1}H NMR spectrum of PEG-*b*-PSMA, in which the signal (b) at 6.96–7.53 ppm was assigned to the phenyl-ring protons on the block PSMA. The mean degree of polymerization (DP) of the PSMA block of 26 was determined by comparing the integration ratio of signal (d) to signal (c) associated with the methene protons of mPEG. Meanwhile, it can be seen that PEG-*b*-PSMAn had a unimodal curve with relatively low polydispersity and shifted toward a higher molecular region, further confirming the successful synthesis of the block copolymer PEG-*b*-PSMAn (Fig. 1E). For linking the anthracene groups onto the backbone of PEG-*b*-PSMAn *via* reductive disulfide bonds, An-SS-NH_2 was synthesized and characterized by ^{1}H NMR (Fig. S1–3†). According to the ^{1}H NMR spectra (Fig. 1D), the characteristic signals attributed to the anthracene (f, e and d) and TEMPO groups (a) can be seen clearly, indicating the successful introduction of them onto the polymeric backbone. FT-IR analysis further verifies the successful preparation of the targeted copolymers (Fig. S4†). As compared with the spectrum of mPEG-RAFT, the characteristic signal at 1830 cm^{-1} assigned to the MAH units can be seen clearly in that of mPEG-*b*-PSMAn. In the spectrum of mPEG-*b*-P(SMA(-TEMPO)-SS-An (Fig. S4C†), the signal at 1830 cm^{-1} almost disappeared, while the signals at 1680 cm^{-1} and 1030 cm^{-1}, which correspond to the characteristic signals of imide and anthracene groups, respectively, can be seen clearly.

Self-assembly behavior, morphological and optical characterization of PPTIU nanocomposites

The anthraquinone structures in PPT copolymers could be dimeric crosslinked under ultraviolet light, which provided support for the slow release of loaded drugs. In order to explore whether the polymer with anthraquinone has light cross-linking response characteristics, we detected a change in the UV absorption peak of the copolymer under gradient time of NIR irradiation based on the optical conversion capability of UCNPs (Fig. 2A), and the obvious UV absorption peak was

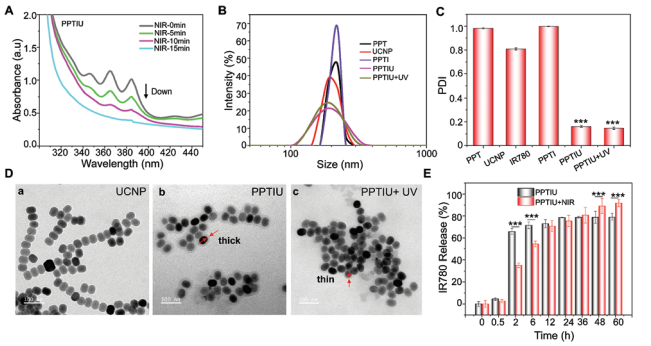

Fig. 2 (A) The absorbance value of polymeric nanocomposites PPTIU with different times of NIR cross-linking. (B) The particle size and (C) polydispersity index (PDI) of the indicated materials by dynamic light scattering (DLS). (D) The transmission electron microscopy (TEM) analysis in UCNPs alone, polymeric nanocomposites with UV irradiation or not. (E) The cumulative IR780 release rate of nanocomposites was determined by HPLC. ***P < 0.001 was considered as the significant difference.

decreased with an increase of the irradiation time. A similar result was also obtained at different times of UV cross-linking (Fig. S5†). The ultraviolet response crosslinking of an anthracene-based PPT copolymer gave it the potential of becoming a photocontrolled sustained-release drug carrier. Therefore, based on this PPT copolymer, UCNP and IR780 were loaded to form a nanocomplex by the solvent volatilization method, expecting to achieve near-infrared controlled drug release. The nanocomposites obtained by the PPT copolymer loaded with IR780 alone were defined as PPTI, and the nanocomposites loaded with IR780 and UCNPs were defined as PPTIU. As shown in Fig. 2B, the PPT copolymers loaded with UCNPs and IR780 have uniform particle sizes, the hydrated particle size of which is about 200 nm. The PPTIU nanocomposites had a significantly lower particle size dispersion index (PDI) than the PPTI nanocomposites (Fig. 2C), indicating that the incorporation of UCNPs gave good stability to the nanocomposites. The stability of the PPTIU nanocomposites was also confirmed in Fig. S6.† After 48 h of incubation at 37 °C, both the PPTIU nanocomposites with and without UV irradiation showed stable size dispersion. The detailed morphological feature was also evaluated using a transmission electron microscope (TEM), and the polymer layer on the surface of UCNPs acted as a polymeric shell structure (Fig. 2D). More interestingly, the polymer shell was obviously thinner when UV-light induction, and the UV-induced anthracene-crosslinking might contribute to the structure conversion. Besides, considering IR780 as a photosensitizer with excellent photodynamic and photothermal treatment effects, and anthracene-crosslinked materials show poor heat resistance and dissociate at high temperature. Then, in order to investigate whether the photothermal effect of IR780 would interfere with the anthracene-crosslinking of PPTIU nanocomposites, as shown in Fig. S7†, the PPT copolymer was treated with UV for 5 min, and the crosslinked-copolymers were further heated to 45 °C or 60 °C, and the anthra-

cene-specific UV absorption peak was preserved, which proved that the photothermal effect of IR780 cannot interfere with the crosslinking state of the PPT copolymer. To further validate the potential of the photocontrolled sustained-release drug carrier, the role of the anthracene-crosslinking effect was analyzed using a dialysis test. As shown in Fig. S8†, the PPTIU with NIR group could effectively maintain micelle stability for 24 h, while the no NIR group represents some particle precipitation. Based on the excellent stability of NIR-crosslinked nanocomposites, the sustained drug delivery capacity was also detected by the cumulative drug release in Fig. 2E. Anthracene was composed of three linear aromatic rings, which could undergo an anthracene dimerization reaction under an ultraviolet trigger to form anthracene crosslinked polymers, and the crosslinking product was relatively stable and chemically resistant. Based on this, the PPT polymer could be connected to each other through anthracene crosslinking, which resulted in IR780 locked in the cavity of the cross-linked polymer, so as to realize the sustained release of IR780. In detail, the PPTIU nanocomposite group with no NIR-treatment released 63% of IR780 in 2 h and reached a maximum of 78% within 1 day, while the PPTIU nanocomposite group with NIR-treatment released only 35% of IR780 in 2 h, the cumulative release was higher than 91%, indicating that NIR-triggered anthraquinone chemical crosslinking could effectively improve IR780 sustained release, which is a commonly accepted strategy to increase the bioavailability of pharmaceutics for improvement of cancer therapy.

Moreover, the successful co-loading of UCNPs and IR780 was also evaluated. With an increase of the PPT copolymer and UCNP ratio, the fluorescence intensity of enveloped IR780 gradually decreased and showed a red-shift phenomenon, which indicated that the PPT polymer could be successfully loaded with IR780 and the fluorescence capacity was maintained (Fig. 3A). The UV absorption analysis also showed a specific peak of the PPT copolymer and IR780, which further demonstrated the successful assembly of nanocomposites (Fig. 3B). Besides, after the incorporation of TEMPO, a magnetic resonance radical,[22–24] the T1 magnetic resonance imaging capacity of PPTIU nanocomposites was evaluated as in Fig. 3C. The MRI ability was enhanced with an increase in the concentration of the PPT copolymer. The relaxation time was determined according to the mapping module, and the correlation value was higher than 0.99 (Fig. 3D), indicating the excellent T1-MRI capacity of PPTIU nanocomposites, which could be applied in the tracking of nanocomposites *in vivo* without the limitation of the tissue penetration depth.

In vitro cellular uptake and toxicity evaluation of PPTIU nanocomposites

In order to investigate whether the PPTIU polymer could mediate the uptake of IR780 by tumor cells, we characterized the cellular uptake amount of IR780 using laser confocal microscopy and flow cytometry (Fig. 4A and B). Compared to the low fluorescence intensity of IR780 alone, the PPTIU group showed enhanced IR780 fluorescence for 1 h of treatment and

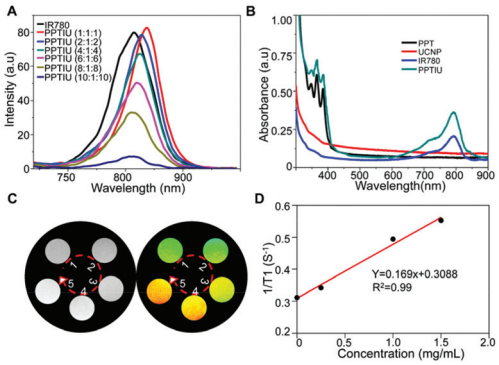

Fig. 3 (A) The fluorescence intensity of free IR780 and nanocomposites with different packaging ratios. (B) The absorbance value of IR780, UCNPs, and nanocomposites with IR780 loading. (C) The T1 magnetic resonance imaging and (D) T1 relaxation time of polymeric nanocomposites with different concentrations of polymers by Bruker BioSpec 9.4T Animal MRI.

partial cellular uptake at 0.5 h. Quantitative flow cytometry results also showed that the cellular uptake amount of the PPTIU polymer was 1.8 times that of IR780 alone. Due to the PDT response of IR780, we also used an H2DCFDA probe to verify the *in vitro* ROS release level of the nanocomposite in HepG2 cells. It could be evaluated from Fig. 4C that the H2DCFDA fluorescence generated by ROS from the PPTIU nanocomposite under NIR light for 5 min was stronger than that generated by no laser excitation or the IR780 plus NIR group. The difference could be seen more intuitively from the quantitative analysis in Fig. S9.† The quantitative fluorescence value in Fig. 4D also directly indicated that the PPTIU plus NIR group could effectively produce ROS and realize PDT. In order to verify the *in vitro* cytotoxicity of the polymer and nanocomplex, LO2 cells, HEK293T cells and HepG2 cells were cultured, and the toxicity of PPT and UCNPs was respectively verified using the MTT assay (Fig. S10A, B and C†). It could be seen that the toxicity of PPT and UCNPs to cells was relatively low, and the cell viability at a concentration of 50 μg mL^{-1} were both higher than 90%. Meanwhile, IR780 had photothermal therapy properties that could induce tumor cell death, so we also evaluated the cell viability of IR780, PPTI and PPTIU against HepG2 cells under near-infrared light excitation (Fig. 4E). The PPTIU plus NIR group showed the strongest cytotoxicity, and the cytotoxicity of HepG2 cells was as low as 17.8% when the concentration of IR780 in the PPTIU nanocomposite reached 5 μg mL^{-1}. However, it was worth noting that PPTIU also has certain cell lethality, mainly because IR780 itself also had certain tumor cytotoxicity, and the temperature increase triggered by a NIR laser would further aggravate the cell death.[25,26]

In vivo bimodal imaging and photothermal effect of the nanocomposites

Precise tracking is essential to drug administration, and imaging-guided treatment solutions have significant advan-

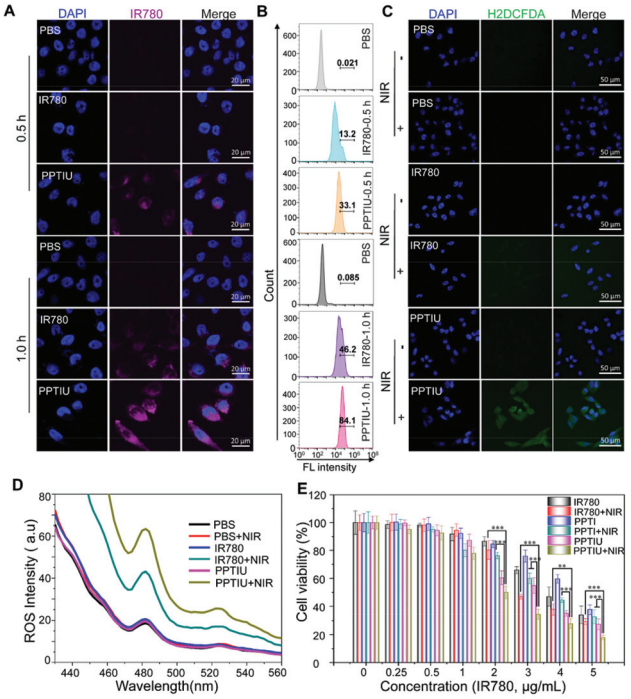

Fig. 4 (A) The cellular uptake of IR780 in HepG2 with free IR780 and IR780-loaded polymeric nanocomposites by confocal microscopy and (B) flow cytometry. (C) The ROS production was determined with an H2DCFDA probe by confocal microscopy and (D) fluorescence spectral analysis. (E) The HepG2 cells were treated with free IR780 or polymeric nanocomposites with NIR irradiation or not, and the cell viability was evaluated by MTT. $^{**}P < 0.01$ and $^{***}P < 0.001$ were considered as the significant difference.

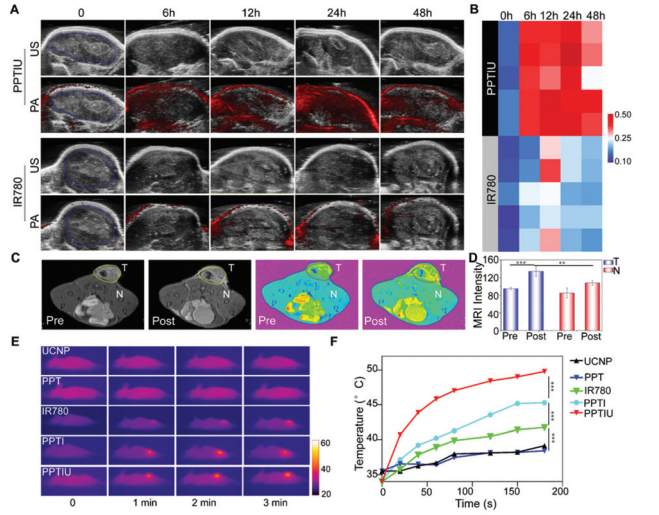

Fig. 5 (A) *In vivo* IR780 tumor uptake between free IR780 and polymeric nanocomposites was subjected to photoacoustic imaging, and (B) the photoacoustic intensity was determined by the ROI intensity. (C) *In vivo* magnetic resonance contrast ability of polymeric nanocomposites in HepG2 subcutaneous tumors before or after intravenous injection and (D) the T1 contrast imaging in tumor and normal tissues were conducted with the ROI value. (E and F) The photothermal activity of different materials in HepG2-bearing nude mice after 6 h of intravenous injection was recorded by infrared imaging equipment. $^{**}P < 0.01$ and $^{***}P < 0.001$ were considered as the significant difference.

tages in cancer therapy, including drug dosage control, choice of treatment time and combination therapy control.[27] To validate the fluorescence performance of IR780, photoacoustic imaging (PAI) was conducted in a HepG2-bearing tumor model by vein injection. As shown in Fig. 5A and B, the photoacoustic imaging capacity of PPTIU was significantly higher than free IR780, and 24 h of administration of PPTIU represented the highest photoacoustic imaging *in vivo*. Due to the rapid clearance and the instability of most photosensitizers, including FDA-approved ICG and IR780. Therefore, the group with free IR780 showed poor photoacoustic imaging capacity *in vivo*, and the uniform dispersibility and good stability of PPTIU were demonstrated as mentioned above, showing good sustained drug release, and thus enhanced the drug retention in tumors. Meanwhile, the main organs and tumors were collected after 48 h of administration of PPTIU, and then subjected to fluorescence imaging, and the data showed that the fluorescence signaling was mostly located in the tumor tissues after 48 h of administration (Fig. S11†), indicating that PPTIU nanocomposites exhibited good tumor passive targeting ability and good metabolic behavior, which could enhance the tumor therapeutic effect and decrease the toxicity risk to normal tissues. Moreover, magnetic resonance imaging without tissue depth limitation was also evaluated, and the results demonstrated that the T1 imaging intensity was increased after PPTIU injection (Fig. 5C). More importantly, the MRI intensity in tumors was also remarkably greater than normal tissues (Fig. 5D), indicating the better tumor-passive targeting capacity of PPTIU nanocomposites, which could provide a strategy for tumor magnetic resonance imaging. Compared to the first-generation gadolinium agents and second-generation superparamagnetic iron oxide (SPIO) nanoparticles, the TEMPO-based polymers exhibited superior biocompatibility and biodegradability, behaving the lower cytotoxicity than gadolinium agents and the higher resolution T1 imaging than T2 imaging features. Benefitting from the passive-targeting drug delivery in 24 h, the photothermal assay was conducted after vein injection. As shown in Fig. 5E and F, the PPT-loading could significantly increase the efficacy of PTT than free IR780, UCNPs or the PPT copolymer. More interestingly, the incorporation of UCNPs into the PPT copolymer can also show a better photothermal effect than PPTI, indicating that NIR-induced anthracene-crosslinking not only regulates the drug release, but also enhances the photothermal conversion efficiency.

Evaluation of the *in vivo* therapeutic efficacy of PPTIU nanocomposites

The HepG2 solid tumor model in nude mice was selected to explore the *in vivo* therapeutic effect of the PPTIU nanocomplex, and then the nanocomplexes were injected intratumorally 7 days after vein injection, for which the injection content of

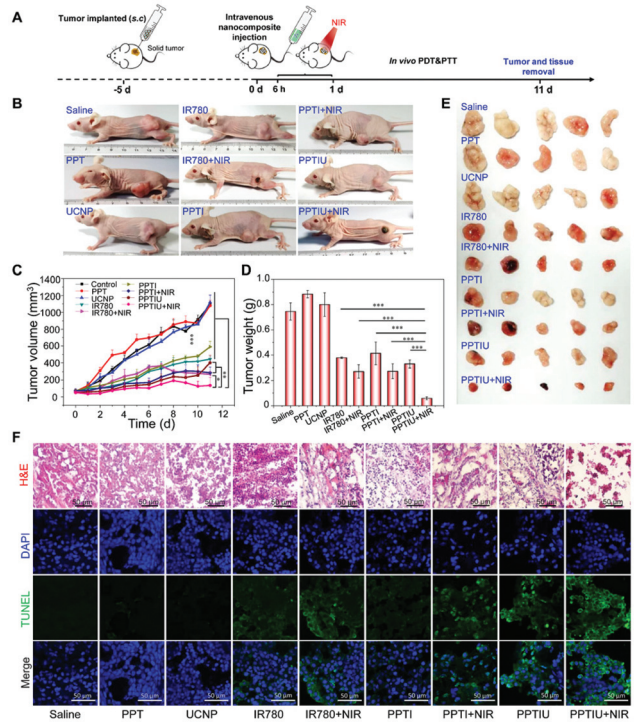

Fig. 6 (A) The description of the *in vivo* nude mouse HepG2-bearing tumor scheme. (B) After 11 days of treatment, the tumor imaging was recorded using a photographic camera. (C) The tumor volume was recorded during the period of treatment. (D and E) The nude mouse was sacrificed and the tumors were excised; the tumor weight and tumor images were recorded. (F) The tumor tissues in different groups were subjected to H&E staining and TUNEL staining. $*P < 0.05$, $**P < 0.01$ and $***P < 0.001$ were considered as the significant difference.

PPT and UCNPs was 10 mg kg^{-1}, and the injection content of IR780 was 1 mg kg^{-1} (Fig. 6A). As shown in Fig. 6B and E, tumor morphology in the nude mice was recorded and tumor tissues were dissected respectively. It was noteworthy that the skin in the NIR irradiation group showed different degrees of the scald phenomenon, which was mainly due to the heating caused by the photothermal effect of IR780. The PPTIU plus NIR group exhibited the best therapeutic effect. The tumor volume of the PPTIU plus NIR group was basically maintained at about 100 mm^3, and the tumor volume has decreased by 90.9% compared to the control group (Fig. 6C). Similar results were also confirmed in the tumor weight evaluation (Fig. 6D). Of note, the group with free IR780 plus NIR also showed a therapeutic effect, and the physical toxicity and the photothermal treatment effect of IR780 itself might contribute to the result. In order to evaluate the pharmaceutical effect, H&E staining and TUNEL immunofluorescence staining (Fig. 6F) demonstrated the best pharmaceutical effect of PPTIU nanocomposites, followed by the PPTI plus NIR and PPTIU group. Due to the toxicity of IR780 itself, efficient cellular delivery in PPTIU without NIR also induced cell apoptosis or necrosis.

Based on the toxicity of anthraquinone structure, the *in vivo* toxicity of PPT copolymers has attracted much more attention.

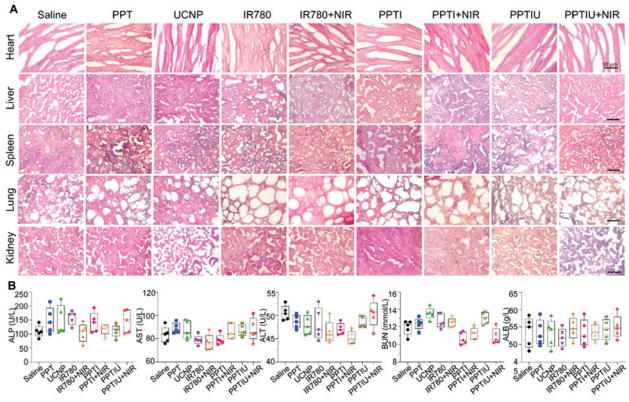

Fig. 7 (A) The biosafety assessment in different organs by H&E staining and (B) biochemical indicators of the liver, kidneys and heart.

In order to assess the polymer structure and *in vivo* toxicity of IR780, the specific morphology of the heart, liver, spleen, lungs, and kidneys were assessed by H&E staining (Fig. 7A). By comparing the PPT polymer group with the control group, we could not find any significant difference, indicating that PPT polymer had little impact on the heart, liver, spleen, lungs and kidneys of nude mice, so we could initially think that the PPT polymer can be used for *in vivo* drug delivery. In addition, PPTIU and PPTIU plus NIR groups also did not find obvious tissue toxicity, which proved that loading IR780 iodide with nanocomposites could achieve the effect of photothermal, photodynamic and chemotherapy treatment on tumors while reducing the toxicity on normal tissue, thus further verifying the safety of PPTIU nanocomposites. In addition, the biochemical indicators of liver, kidney and heart function were determined by serum evaluation. ALP, AST and ALT are three biochemical indicators of liver function, and it was found that there was no significant difference between the liver biochemical indicators of the PPTIU plus NIR group and the control group, indicating that the PPTIU plus NIR group did not cause liver toxicity. Similarly, we did not find a significant difference between the PPTIU plus NIR group and the control group by comparing the renal biochemical indicators and cardiac indicators (Fig. 7B), and the mouse weight also showed no significant difference (Fig. S11†). The pharmaceutical effect of PPTIU nanocomposites was achieved by *in situ* photothermal and photodynamic combination tumor therapy, which has no remarkable toxicity in normal tissues, indicating that the PPT copolymer has the potential to become a safe drug delivery system.

Conclusions

In summary, we successfully developed an anthracene-functionalized copolymer with a magnetic resonance radical (TEMPO). Upon co-loading of the photosensitizer IR780 and upconversion nanoparticles (UCNPs), a nanocomposite with a shell–core structure can be achieved by near-infrared (NIR)-

crosslinking. The crosslinking endowed the nanocomposites with stability, leading to sustained drug release and enhanced drug retention. More importantly, bimodal imaging involving magnetic resonance imaging (MRI) and photoacoustic imaging (PAI) favours the monitoring function and guides the PTT/PDT process for cancer therapy.

Conflicts of interest

There are no conflicts to declare.

Acknowledgements

This work was supported by the Major State Basic Research Development Program of China (2017YFA0205201 and 2018YFA0107301), the National Natural Science Foundation of China (NSFC) (81901876 and U1705281) and the Agency for Science, Technology and Research (A*STAR) under its AME IAF-PP Specialty Chemicals Programme (Grant No. A1786a0034). All animal experiments were approved by the Animal Management and Ethics Committee of Xiamen University.

Notes and references

1 M. Li, Y. Shao, J. H. Kim, Z. Pu, X. Zhao, H. Huang, T. Xiong, Y. Kang, G. Li and K. Shao, *J. Am. Chem. Soc.*, 2020, **142**, 5380–5388.
2 C. Chu, J. Yu, E. Ren, S. Ou, Y. Zhang, Y. Wu, H. Wu, Y. Zhang, J. Zhu and Q. Dai, *Adv. Sci.*, 2020, **7**, 2000346.
3 Y. Jiang, X. Zhao, J. Huang, J. Li, P. K. Upputuri, H. Sun, X. Han, M. Pramanik, Y. Miao and H. Duan, *Nat. Commun.*, 2020, **11**, 1–13.
4 C. Chu, E. Ren, Y. Zhang, J. Yu, H. Lin, X. Pang, Y. Zhang, H. Liu, Z. Qin and Y. Cheng, *Angew. Chem., Int. Ed.*, 2019, **58**, 269–272.
5 X. Wang, Z. Xuan, X. Zhu, H. Sun, J. Li and Z. Xie, *J. Nanobiotechnol.*, 2020, **18**, 1–19.
6 Y. Wang, P. Zhang, Y. Wei, K. Shen, L. Xiao, R. J. Miron and Y. Zhang, *Adv. Healthcare Mater.*, 2021, **10**, 2001014.
7 E. B. Ehlerding, X. Lan and W. Cai, *Theranostics*, 2018, **8**, 812.
8 Q. Dai, E. Ren, D. Xu, Y. Zeng, C. Chen and G. Liu, *Progress in Natural Science: Materials International*, 2020.
9 Z. Hu, C. Fang, B. Li, Z. Zhang, C. Cao, M. Cai, S. Su, X. Sun, X. Shi and C. Li, *Nat. Biomed. Eng.*, 2020, **4**, 259–271.
10 H. Chen, H. Cheng, Q. Dai, Y. Cheng, Y. Zhang, D. Li, Y. Sun, J. Mao, K. Ren and C. Chu, *J. Controlled Release*, 2020, **323**, 635–643.
11 X. Li, J. F. Lovell, J. Yoon and X. Chen, *Nat. Rev. Clin. Oncol.*, 2020, **17**, 657–674.
12 S. Yan, X. Zeng, Y. A. Tang, B. F. Liu, Y. Wang and X. Liu, *Adv. Mater.*, 2019, **31**, 1905825.
13 Y. Wang, W. Wu, J. Liu, P. N. Manghnani, F. Hu, D. Ma, C. Teh, B. Wang and B. Liu, *ACS Nano*, 2019, **13**, 6879–6890.
14 S. Kwon, H. Ko, D. G. You, K. Kataoka and J. H. Park, *Acc. Chem. Res.*, 2019, **52**, 1771–1782.
15 H. S. Jung, P. Verwilst, A. Sharma, J. Shin, J. L. Sessler and J. S. Kim, *Chem. Soc. Rev.*, 2018, **47**, 2280–2297.
16 C. Li, W. Zhang, S. Liu, X. Hu and Z. Xie, *ACS Appl. Mater. Interfaces*, 2020, **12**, 30077–30084.
17 Z. Hou, W. M. Nau and R. Hoogenboom, *Polym. Chem.*, 2021, **12**, 307–315.
18 K. Jin, A. Banerji, D. Kitto, F. S. Bates and C. J. Ellison, *ACS Appl. Mater. Interfaces*, 2019, **11**, 12863–12870.
19 J. Xu, A. Gulzar, Y. Liu, H. Bi, S. Gai, B. Liu, D. Yang, F. He and P. Yang, *Small*, 2017, **13**, 1701841.
20 Y.-C. Tsai, P. Vijayaraghavan, W.-H. Chiang, H.-H. Chen, T.-I. Liu, M.-Y. Shen, A. Omoto, M. Kamimura, K. Soga and H.-C. Chiu, *Theranostics*, 2018, **8**, 1435.
21 N. Rutley and G. Miller, *Pollen and Pollen Tube Biology*, Springer, 2020, pp. 167–179.
22 M. Hou, X. Lu, Z. Zhang, Q. Xia, C. Yan, Z. Yu, Y. Xu and R. Liu, *ACS Appl. Mater. Interfaces*, 2017, **9**, 44316–44323.
23 L. Xia, C. Zhang, M. Li, K. Wang, Y. Wang, P. Xu and Y. Hu, *Int. J. Nanomed.*, 2018, **13**, 7123.
24 Y. Zhu, Y. Matsumura, M. Velayutham, L. M. Foley, T. K. Hitchens and W. R. Wagner, *Biomaterials*, 2018, **177**, 98–112.
25 C. Zhao, Y. Tong, X. Li, L. Shao, L. Chen, J. Lu, X. Deng, X. Wang and Y. Wu, *Small*, 2018, **14**, 1703045.
26 M. Chen, R. O. L. Pérez, P. Du, N. Bhattarai, K. C. McDonough, S. Ravula, R. Kumar, J. M. Mathis and I. M. Warner, *ACS Appl. Mater. Interfaces*, 2019, **11**, 27548–27557.
27 X. Shi, X. Ma, E. Ren, Y. Zhang, D. Jia, Y. Gao, P. Xue, Y. Kang, G. Liu and Z. Xu, *ACS Appl. Mater. Interfaces*, 2019, **11**, 40704–40715.